Developing Lattice Matched ZnMgSe Shells on InZnP Quantum Dots for Phosphor Applications

Mulder, Jence T.; Kirkwood, Nicholas; De Trizio, Luca; Li, Chen; Bals, Sara; Manna, Liberato; Houtepen, Arjan J.

DOI
10.1021/acsanm.0c00583

Publication date
2020

Document Version
Final published version

Published in
ACS Applied Nano Materials

ACS APPLIED NANO MATERIALS

www.acsanm.org

Article

Developing Lattice Matched ZnMgSe Shells on InZnP Quantum Dots for Phosphor Applications

Jence T. Mulder, Nicholas Kirkwood, Luca De Trizio, Chen Li, Sara Bals, Liberato Manna, and Arjan J. Houtepen*

Cite This: *ACS Appl. Nano Mater.* 2020, 3, 3859−3867

Read Online

ACCESS | Metrics & More | Article Recommendations | Supporting Information

ABSTRACT: Indium phosphide quantum dots (QDs) have drawn attention as alternatives to cadmium- and lead-based QDs that are currently used as phosphors in lamps and displays. The main drawbacks of InP QDs are, in general, a lower photoluminescence quantum yield (PLQY), a decreased color purity, and poor chemical stability. In this research, we attempted to increase the PLQY and stability of indium phosphide QDs by developing lattice matched InP/MgSe core−shell nanoheterostructures. The choice of MgSe comes from the fact that, in theory, it has a near-perfect lattice match with InP, provided MgSe is grown in the zinc blende crystal structure, which can be achieved by alloying with zinc. To retain lattice matching, we used Zn in both the core and shell and we fabricated InZnP/$Zn_xMg_{1-x}Se$ core/shell QDs. To identify the most suitable conditions for the shell growth, we first developed a synthesis route to $Zn_xMg_{1-x}Se$ nanocrystals (NCs) wherein Mg is effectively incorporated. Our optimized procedure was employed for the successful growth of $Zn_xMg_{1-x}Se$ shells around In(Zn)P QDs. The corresponding core/shell systems exhibit PLQYs higher than those of the starting In(Zn)P QDs and, more importantly, a higher color purity upon increasing the Mg content. The results are discussed in the context of a reduced density of interface states upon using better lattice matched $Zn_xMg_{1-x}Se$ shells.

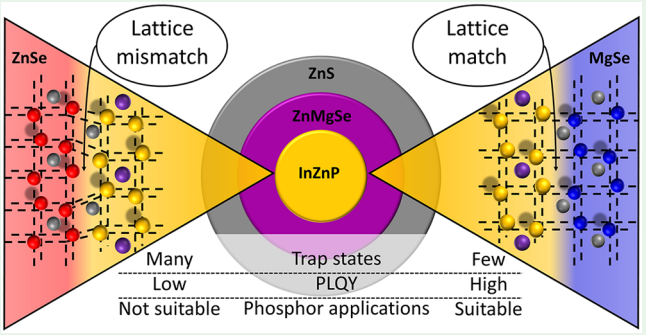

KEYWORDS: *quantum dots, InP, core−shell, lattice matching, phosphor, MgSe*

INTRODUCTION

Quantum dots (QDs) are semiconductor nanocrystals that exhibit unique, size-dependent optical and electrical properties.[1] This makes QDs very interesting for various optoelectronic applications. Currently, QDs are applied as phosphors in displays and lamps,[2−6] and they are further investigated for, among others, solar cells[7,8] and several types of sensors.[9,10] Also, QDs can be used as biological labels for *in vivo* tracking.[11,12]

The main drawback of currently used QDs is their toxicity. The QDs with the highest photoluminescence quantum yield (PLQY) and color purity are all based on cadmium or lead.[13−16] Because of the high toxicity of these metals, their use is restricted or banned from the use in consumer products.[17] Hence, there is an active search to find alternatives for cadmium- and lead-based QD materials.[18−21] One of the best candidates is indium phosphide (InP). Much has been tried to optimize InP QDs by both computational[16] and experimental work.[5,6,22−27] However, in terms of color purity and chemical stability, these QDs (maximum reported full width at half-maximum (FWHM) of 35 nm)[27] are not yet on par with Cd-based QDs (maximum reported FWHM of 20 nm).[28−30]

QDs with a high PLQY and good stability are generally formed by growing a protective shell around the core of the emitting material. The shell passivates possible in-gap states on the surface of the emitting core. Furthermore, the shell protects the QD core from hydrolysis and oxidation. Requirements for a well-passivating shell are a type I band alignment for the shell material (i.e., the valence band should be lower and the conduction band higher in energy for the shell material than the core material), a matching crystal structure, and a good match in lattice parameters between the core and the shell material.[31] If there is no type I band alignment, delocalization of charge carriers from the core to the shell occurs. This leads to trapping of charge carriers in in-gap states on the shell surface and hence a reduction of the PLQY.[31] If the lattice parameters of both materials do not

Received: February 28, 2020
Accepted: March 16, 2020
Published: March 16, 2020

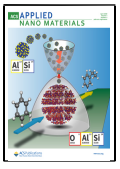

match, epitaxial shell growth is not possible, resulting in interfacial defects that can form trap states.

Growing epitaxial shells has been the main challenge in developing high quality InP QDs. Zinc sulfide (ZnS), which is most commonly used as a shell material, has a −7.8% lattice mismatch with the InP core (Table 1), which leads to a low

Table 1. Material Properties of InP and Different Shell Materials[a]

material	crystal structure	lattice parameter (Å)	mismatch vs InP (%)	bulk band gap (eV)	band alignment
InP	zinc blende	5.87		1.34	
ZnS	zinc blende	5.41	−7.8	3.78	type I
ZnSe	zinc blende	5.67	−3.4	2.82	type I
MgSe	zinc blende	5.90	0.51	4.05	type I[34]
MgSe	rock salt	5.46	−7.0	2.53[35]	quasi-type II to type I

[a]All values were taken from ref 33 if not indicated differently.

PLQY.[32] ZnSe matches better, with a −3.4% mismatch, and very recent work has shown >90% PLQY for InP/ZnSe/ZnS QDs.[25,26] However, on paper, the best lattice match can be achieved with zinc blende MgSe, which has a lattice mismatch of 0.5%. Furthermore, MgSe is a wide bandgap material (∼4 eV) assuring a type I band alignment with InP (see Table 1).[33] This has motivated us to investigate the possibility of growing lattice matched MgSe shells onto InP QDs.

A challenge is that the native crystal structure of MgSe is not zinc blende but rock salt,[33,36] resulting in a significant lattice mismatch with InP. Potentially MgSe could adopt the zinc blende crystal structure when grown epitaxially on zinc blende InP QDs. However, our attempts to do so where unsuccessful. On the other hand, by alloying MgSe with zinc, $Zn_xMg_{1-x}Se$ can be formed with a zinc blende crystal structure.[36] Therefore, we attempted to grow $Zn_xMg_{1-x}Se$, protected by a ZnS shell, as a novel shell material around InP QDs, as illustrated in Figure 1. For simplicity, from now on we will refer to this $Zn_xMg_{1-x}Se$ alloy as ZnMgSe. To compensate for the smaller lattice parameter of ZnMgSe compared to that of MgSe, we included a small fraction of Zn in the InP cores, termed InZnP, so that the core lattice parameter could be also reduced.[32,37] This way it would be possible to, in theory, achieve a perfect core−shell lattice match.

EXPERIMENTAL METHODS

Methyl acetate (anhydrous, 99.5%), toluene (anhydrous, 99.8%), 1-octadecene (ODE, technical grade, 90%), tris(trimethylsilyl)-phosphine (PTMS, 95%), trioctylphosphine (TOP, 97%), selenium (99.99%), palmitic acid (HPA, >99%), indium acetate ($In(Ac)_3$, 99.99% trace metal basis), zinc acetate ($Zn(Ac)_2$, 99.99% trace metal basis), diethylzinc (≥52 wt % Zn basis), and di-*n*-butylmagnesium (1 M in heptane) were purchased from Sigma-Aldrich. Ethanol (absolute, SupraSolv for GC-EDC/FID) was purchased from Merck. Oleylamine (OLA, 80−90% C18, ≥96.0% (primary amine)) was purchased from Acros Organics. *n*-Hexane (anhydrous) and sulfur (Puratronic , 99.9995%) were purchased from Alfa Aesar.

The used tris(trimethylsilyl)phosphine, diethylzinc, and di-*n*-butylmagnesium are spontaneously reactive with air and moisture and should therefore be handled with care and solely under inert atmosphere.

Overview of All Samples Discussed in This Work. Many different types of samples are discussed and compared in this work. For clarity, we list all different types in Table 2 together with the Figure they are discussed in. In this work the mentioned Mg fractions always relate to the Mg feed fraction, unless stated differently.

Table 2. List of All Samples Used in the Figures Displayed in This Article

sample type	core	1st shell	2nd shell	displayed in	analysis performed
1	Zn(Mg)Se	ZnS		Figure 2	optical (a), XRD (b)
2	InZnP	Zn(Mg)Se		Figure 3	TEM (a−e), ICP (f), XPS (f)
2	InZnP	Zn(Mg)Se		Figure 5	optical (e, f)
3	InZnP	Zn(Mg)Se (thicker)	ZnS (thinner)	Figure 4	XRD (a−c)
4	InZnP	Zn(Mg)Se	ZnS	Figure 5	optical (a−f)

Synthesis of InZnP Core Quantum Dots by the Heating-Up Method. The core synthesis method is adapted from the heating-up procedure of Ramasamy et al.[38] In short, 44 mg of $In(Ac)_3$ (0.15 mmol), 14 mg of $Zn(Ac)_2$ (0.075 mmol), 147 mg of HPA (0.575 mmol), and 5 mL of ODE were added to a suitable three necked flask. Subsequently, the flask was attached to a Schlenk line and heated to 120 °C while stirring at 800 rpm. When the contents reached 120 °C, the flask was put under a vacuum of 1 mbar to remove water and oxygen from the reaction mixture. After 1 min, the flask was put under dry nitrogen and then back under vacuum to purge the mixture further. This purging process was repeated for a total of three times. Afterward, the flask was put under vacuum at 120 °C overnight, to completely remove any residual water and oxygen as well as any acetic acid that formed. Then, the flask was put back under nitrogen to atmospheric pressure and cooled to 50 °C, and under a continuous flow of nitrogen 29 μL (0.1 mmol) of PTMS dissolved in 1 mL of TOP was injected while stirring at 800 rpm. After injection, the temperature was increased with increments of 5 °C every 20 s until it reached 305 °C. The flask was kept stirring for 2 min at this temperature, before it was rapidly cooled to 80 °C by the use of

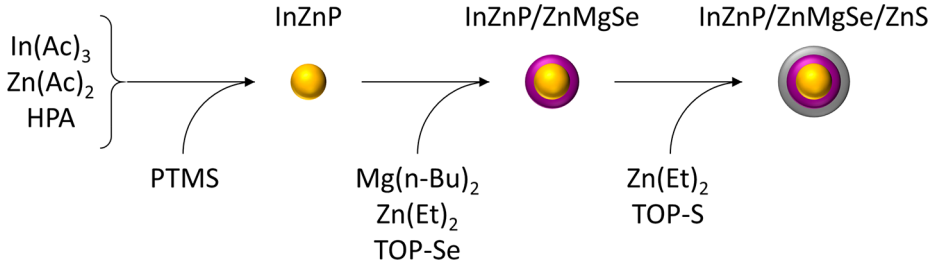

Figure 1. Schematic of the synthesis steps taken in the synthesis of InZnP/ZnMgSe/ZnS QDs.

https://dx.doi.org/10.1021/acsanm.0c00583
ACS Appl. Nano Mater. 2020, 3, 3859−3867

compressed air. Thereafter, 2 mL of anhydrous toluene was injected to facilitate the transfer of the solution from the flask to a vial, which was filled with nitrogen prior to use. The solution was brought into a glovebox, and ethanol was added as antisolvent until the reaction mixture became turbid, which indicated the precipitation of the formed quantum dots. The quantum dot precipitate was centrifuged for 15 min at a relative centrifugal force of 1800*g*, and subsequently the supernatant was removed under an inert atmosphere. The quantum dot cores, often found as an oily orange droplet, were redispersed in 1 mL of anhydrous hexane.

Synthesis of ZnMgSe Nanocrystals. The synthesis method for ZnMgSe NCs is adapted from the synthesis of ZnSe NCs by Boldt et al.[39] In a 25 mL three-necked flask, 8.61 mL (7 g) of degassed OLA was stirred and heated to 300 °C. When the contents reached 300 °C, 785 μL of 1 M TOP-Se (in TOP) with an additional 1.6 mL of TOP was injected. Immediately after, a total of 785 μL of 1 M organometallic compounds (diethylzinc and/or di-*n*-butylmagnesium) was swiftly added. The particles were grown further by the addition of 0.245 mmol of both precursors every 30 min (TOP-Se dissolved in a total of 750 μL of TOP) in the same order as previously described, until the desired size was reached. After the last injection of precursors, the mixture was stirred for another 30 min to anneal any defects. Subsequently, the mixture was cooled rapidly by the use of compressed air, and 2 mL of anhydrous toluene was added. The solution was then transferred to a glovebox, and by the addition of ethanol the particles were precipitated. After centrifuging the solution, the supernatant was decanted, and the particles were resuspended in 1 mL of anhydrous toluene.

To protect the nanoparticles from oxidation and hydrolysis, a ZnS shell was grown around the ZnMgSe NCs. This was done by adding a total of 1 mmol of TOP-S (in TOP) and 1 mmol of diethylzinc ($Zn(Et)_2$) with syringe pumps over the course of 2 h at 200 °C, starting 30 min after the last injection of ZnMgSe precursors.

ZnMgSe and ZnS Shell Growth on InZnP Quantum Dots. To grow ZnMgSe shells around InZnP quantum dot cores, 1 mL of freshly prepared InZnP QD cores in hexane was filtered through a 0.2 μm syringe filter and added to 10 mL of a 1:1 mixture of anhydrous ODE and OLA. The contents were placed in a nitrogen filled flask, attached to a Schlenk line, after which the hexane in the mixture was removed by applying a vacuum for a few minutes. Subsequently, the flask was put back under nitrogen, and the contents were heated to 200 °C. At the moment the solution reached 50 °C, 350 μL of 1 M TOP-Se (in TOP) with an additional 300 μL of TOP and 200 μL of 1 M organometallic precursors (diethylzinc and/or di-*n*-butylmagnesium) in the preferred ratio were added dropwise over the course of 1 h by the use of syringe pumps. The $Zn(Et)_2$ and the TOP-Se were mixed prior to the injection; the di-*n*-butylmagnesium ($Mg(n\text{-}Bu)_2$) was added by a separate syringe. After the injection was completed, the mixture was heated further to 240 °C. Once the temperature was stable, 1 mL of 1 M TOP-S in TOP and 1 mL of 1 M $Zn(Et)_2$ in hexane were added by a syringe pump over the course of 1 h. When all precursors were added completely, the temperature was kept at 240 °C for another 30 min to ensure all precursors reacted and any surface defects were annealed. Subsequently, the reaction mixture was cooled by compressed air, and 2 mL of anhydrous toluene was added to facilitate the transfer of the reaction mixture from the flask to the glovebox by the use of nitrogen-filled vials. Anhydrous methyl acetate was added to the reaction mixture until it became turbid. After centrifuging the mixture for 10 min at a relative centrifugal force of 1800*g*, the supernatant was removed, and the solids were resuspended in 1 mL of toluene. This washing step was repeated for two more times, and the final product was stored in 1 mL of toluene under nitrogen gas in a glovebox.

Structural Characterization. TEM micrographs were acquired with a FEI Technai G2 F20 microscope at 200 kV. Samples for TEM imaging were prepared by drop-casting a toluene solution of QDs onto a carbon-coated copper (400-mesh) TEM grid. HR-STEM micrographs were acquired with a FEI Titan microscope operating at 300 kV. The convergence angle for the electron probe is ∼21 mrad. XRD measurements were performed with a Bruker D8 ADVANCE diffractometer (Co Kα, λ = 0.1789 nm).

Optical Characterization. Optical characterization was performed by using gastight 1 cm quartz cuvettes loaded in a N_2-filled glovebox. Absorbance measurements were acquired by using a PerkinElmer Lambda 365 absorbance spectrometer. Fluorescence spectra were acquired by using an Edinburgh Instruments FLS980 spectrometer. Photoluminescence quantum yields were collected by using a reference dye method with fluorescein in 0.1 M sodium hydroxide in water (λ_{ex} = 465 nm).[40]

Elemental Analysis. ICP-OES was performed on a Prodigy 7 spectrometer (LEEMAN LABORATORIES Ltd.) so that the elemental composition of the synthesized QD solutions could be quantified. The samples were digested overnight in aqua regia prior to the ICP measurements. All chemical analyses performed by ICP-OES were affected by a systematic error of about 5%. The ratio of HCl to HNO_3 was 3:1 (v/v).

The XPS analyses were performed with a Kratos Axis Ultra spectrometer using a monochromatic Al Kα source (20 mA, 15 kV). Survey scan analyses were performed with an analysis area of 300 × 700 μm^2 and a pass energy of 160 eV, whereas high-resolution analyses were performed with a pass energy of 10 eV. Specimens for XPS measurements were prepared by dropping a concentrated NC solution onto a freshly cleaved highly oriented pyrolytic graphite substrate (HOPG, ZYB). Spectra were analyzed by using CasaXPS software (version 2.3.17).

RESULTS AND DISCUSSION

InZnP quantum dots were synthesized by a heat-up method reported by Ramasamy et al.[38] as it allows for a large production of QDs (scale up) with a good size distribution (Figure S1). After their synthesis, the QDs were purified to remove any unreacted precursors that could potentially react during the shell growth and therefore resulting in larger and less well-defined QDs (Figure S2). Initially, we studied the growth of ZnMgSe shells by employing a method similar to the one reported by Ramasamy et al. for growing ZnSe onto InP QDs,[38] in which part of the zinc stearate was substituted for magnesium stearate. Unfortunately, by using of this procedure no Mg was incorporated, and the optical properties were much worse for these shells than for pure ZnSe shells, including strongly increased defect emission (Figure S3). Hence, we sought another method to grow ZnMgSe. Therefore, we first focused on developing a synthesis route to produce ZnMgSe NCs and, subsequently, to employ the optimized reaction conditions for the growth of ZnMgSe shells on InZnP QDs.

ZnMgSe NCs. We first tried to synthesize MgSe NCs using Mg-stearate and TOP-Se, but no reaction occurred. Also, the addition of Mg-stearate to a ZnSe synthesis procedure[41] did not result in any change in lattice parameter as observed by electron diffraction measurements (Figure S4). These results suggested that Mg-stearate is not reactive enough to yield either MgSe or ZnMgSe NCs. Hence, we switched to more reactive organometallic Mg precursors. We synthesized ZnMgSe NCs by adapting a procedure reported by Boldt et al.,[39] and employing diethylzinc ($Zn(Et)_2$), di-*n*-butylmagnesium ($Mg(n\text{-}Bu)_2$), and TOP-Se together with oleylamine, used as both solvent and stabilizing ligand. Various ZnMgSe samples having different compositions were prepared by systematically varying the Zn/Mg precursors ratio. However, we found that these NCs were relatively unstable toward purification, as the samples irreversibly precipitated (Figure S5). To enhance their stability, we grew a thin ZnS shell around these NC cores, forming Zn(Mg)Se/ZnS core/shell NCs, whose absorption spectra are reported in Figure 2a.

https://dx.doi.org/10.1021/acsanm.0c00583
ACS Appl. Nano Mater. 2020, 3, 3859−3867

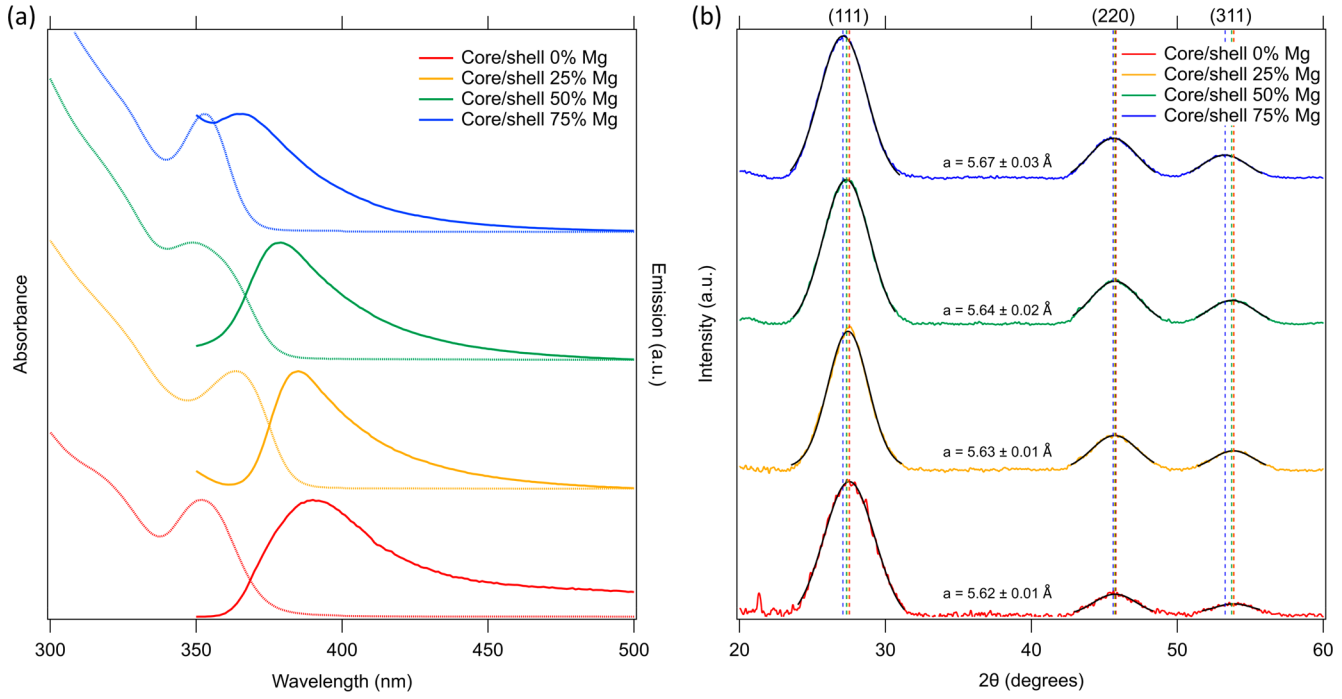

Figure 2. (a) Absorption and emission spectra of Zn(Mg)Se/ZnS NCs synthesized with organometallic precursors with varying feed fractions of Mg(*n*-Bu)$_2$. The spectra are normalized to 1 for the first excitonic peak. (b) XRD diffractograms of Zn(Mg)Se/ZnS NCs synthesized with organometallic precursors with varying feed fractions of Mg(*n*-Bu)$_2$. The lattice parameter values *a* were calculated with Bragg's law, using the peak values of the fits (black lines) for the (111), (220), and (311) crystal planes. The data are normalized to 1 for the (111) reflection peak.

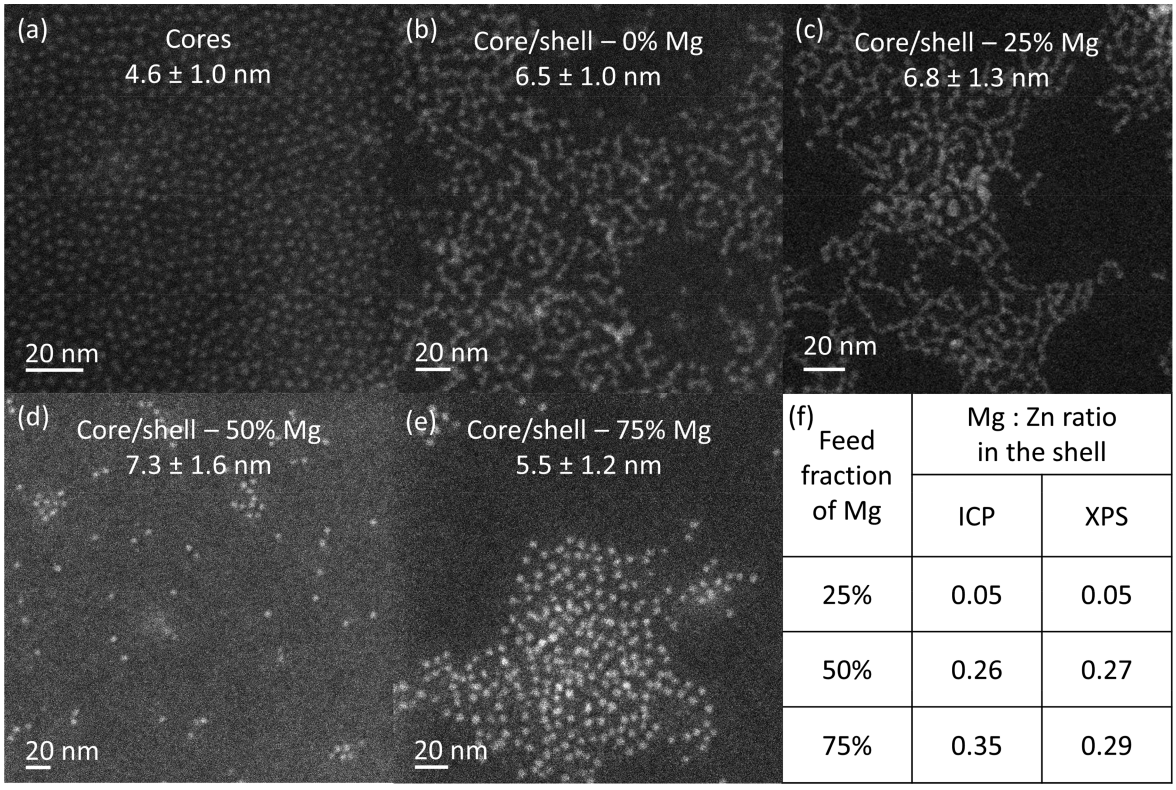

(f)

Feed fraction of Mg	Mg : Zn ratio in the shell	
	ICP	XPS
25%	0.05	0.05
50%	0.26	0.27
75%	0.35	0.29

Figure 3. (a–e) TEM images of the InZnP QD cores and InZnP/Zn(Mg)Se core–shell QDs with a varying Mg(*n*-Bu)$_2$ precursor feed fraction as indicated in the figures. (f) Table of Mg:Zn ratio in the shell measured by ICP and XPS measurements. For all samples, the same cores were used. The amount of Zn in the core (In:Zn 6:1) was subtracted from the core–shell samples to obtain the estimated Mg:Zn ratio in the shell.

Without any Mg, blue emitting and relatively monodisperse ZnSe NCs were formed (red lines in Figure 2a). Upon the addition of Mg(*n*-Bu)$_2$ to the reaction, the first absorption peak initially red-shifted for low feed fractions of Mg (25%), followed by a blue-shift upon further increasing the Mg feed fraction (Figure 2a). On the other hand, emission spectroscopy

https://dx.doi.org/10.1021/acsanm.0c00583
ACS Appl. Nano Mater. 2020, 3, 3859–3867

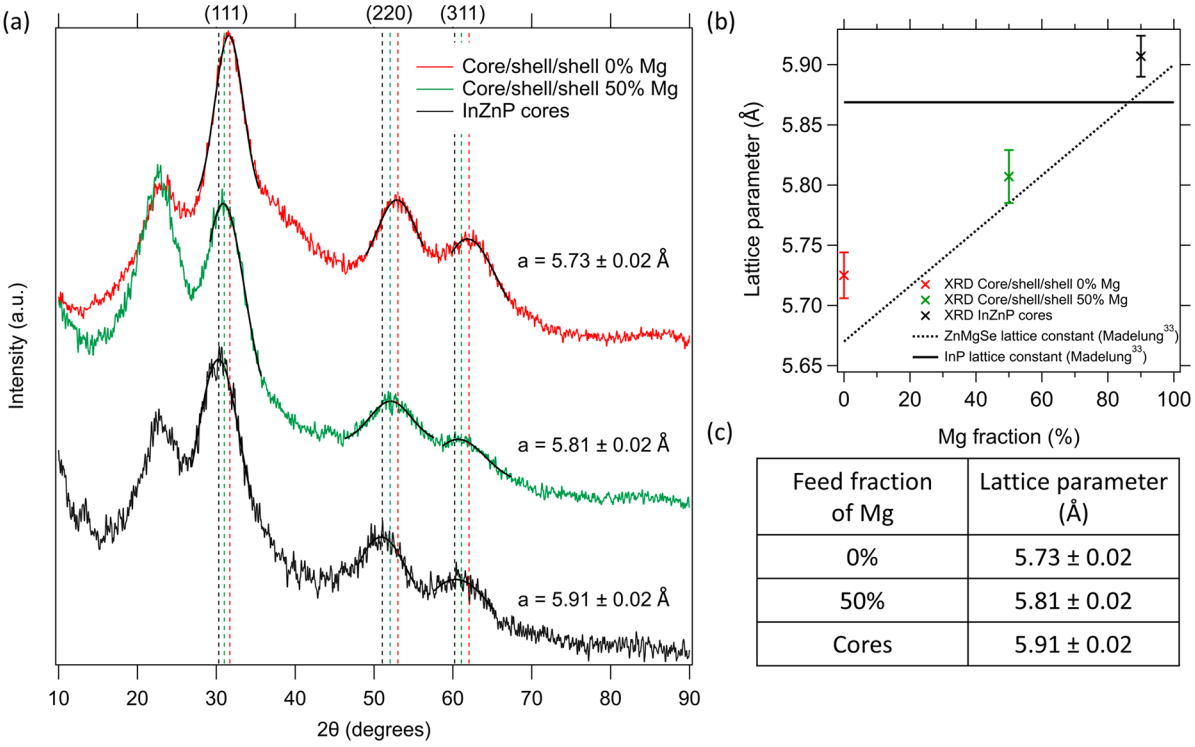

Feed fraction of Mg	Lattice parameter (Å)
0%	5.73 ± 0.02
50%	5.81 ± 0.02
Cores	5.91 ± 0.02

Figure 4. (a) XRD diffractogram of InZnP core and InZnP/Zn(Mg)Se/ZnS core−shell−shell QDs. The shells were synthesized with organometallic precursors with a 0% and 50% fraction of Mg(*n*-Bu)$_2$ in the feed. A clear shift to lower values of 2θ for the Mg containing shells can be observed, indicating a lattice expansion compared to ZnSe, and therefore a better match to the InZnP core. The data are normalized to 1 for the (111) reflection peak. (b) Calculated lattice parameters show a slightly expanded value for the lattice parameter compared to a linearization of the lattice parameters from pure ZnSe and MgSe in the zinc blende structure. The lattice constant for ZnMgSe was obtained from the data from ref 33 and linearly extrapolated following Vegard's law. (c) Calculated values of the lattice parameters of the samples measured in Figure 3a. The lattice parameter values were calculated with Bragg's law by using the peak values of the fits (black lines) for the (111), (220), and (311) crystal planes.

showed a blue-shift for all samples when increasing the Mg feed fraction. This blue-shift was expected, as ZnMgSe should have a higher band gap energy than ZnSe. We note, however, that part of the PL blue-shift is in fact due to a reduced Stokes shift. The initial red-shift of the absorption is most likely related to an increase in particle size. This assumption is strengthened by TEM imaging (Figure S6), which shows that the red-shifted sample has a slightly larger crystallite size. The morphology of the different NCs is furthermore unchanged.

More importantly, the XRD analysis revealed that our reaction conditions led to the formation of ZnMgSe NCs having a zinc blende crystal structure (see Figure 2b). Indeed, the diffractograms showed a slight lattice expansion for the NCs synthesized with a higher Mg feed fraction, indicating the effective inclusion of Mg with the formation of ZnMgSe alloys (see Table 1). This was also observed by EDX analysis, where Mg was found in all ZnMgSe samples (Figure S7).

InZnP/ZnMgSe Core−Shell QDs. InZnP QD cores (with an In:Zn feed ratio of 2:1 and an experimental 6:1 In:Zn ratio determined by ICP-OES and XPS) were added to a 1:1 mixture of degassed ODE and OLA. The organometallic precursors (Mg(*n*-Bu)$_2$, Zn(Et)$_2$) dissolved in heptane and TOP-Se were slowly added to the QD mixture at 200 °C using separate syringe pumps for the Mg(*n*-Bu)$_2$ and the Zn(Et)$_2$/TOP-Se mixture to ensure a controlled shell growth without initiating secondary nucleation of ZnMgSe NCs.

TEM images of the resulting core−shell QDs are presented in Figure 3. All core−shell particles have a larger size compared to the cores and are equal in size within the measurement error for all feed fractions of magnesium. We used XPS and ICP to measure the Mg and Zn contents in all samples. The results are shown in Figure 3f and Figure S8. The measured Mg:Zn ratio matched for both techniques and increased up to a value of ∼30% for a 75% Mg:Zn feed ratio. The combination of similar measured shell thicknesses and the presence of measured Mg through XPS and ICP suggests that in all cases Mg is incorporated into the shell.

InZnP/ZnMgSe/ZnS Core−Shell−Shell QDs. As already stated above for the ZnMgSe NCs, this material is very unstable. To improve the stability, a second, protective ZnS shell was grown around the ZnMgSe shell. This was done by the subsequent injection of Zn(Et)$_2$ and TOP-S to the unpurified reaction mixture containing the core−shell QDs by the use of syringe pumps. We find that the additional ZnS shell strongly increased the colloidal stability of the QDs. In particular, washing of the InZnP/ZnMgSe QDs easily caused irreversible precipitation, while the same samples covered with a ZnS shell could be washed several times (see the Experimental Methods section for details on the washing procedure). The structural and optical analyses below were performed on purified core−shell−shell QDs.

To confirm that the incorporation of Mg still resulted in a zinc blende ZnMgSe shell with the expected lattice expansion, XRD measurements were performed. For the samples with thin Zn(Mg)Se shells shown in Figure 3 (shell radial thickness between 0.5 and ∼1 nm), no clear changes in the XRD diffractograms are observed compared to the core only QDs (see Figure S9). However, samples with thicker shells (tripled

https://dx.doi.org/10.1021/acsanm.0c00583
ACS Appl. Nano Mater. 2020, 3, 3859−3867

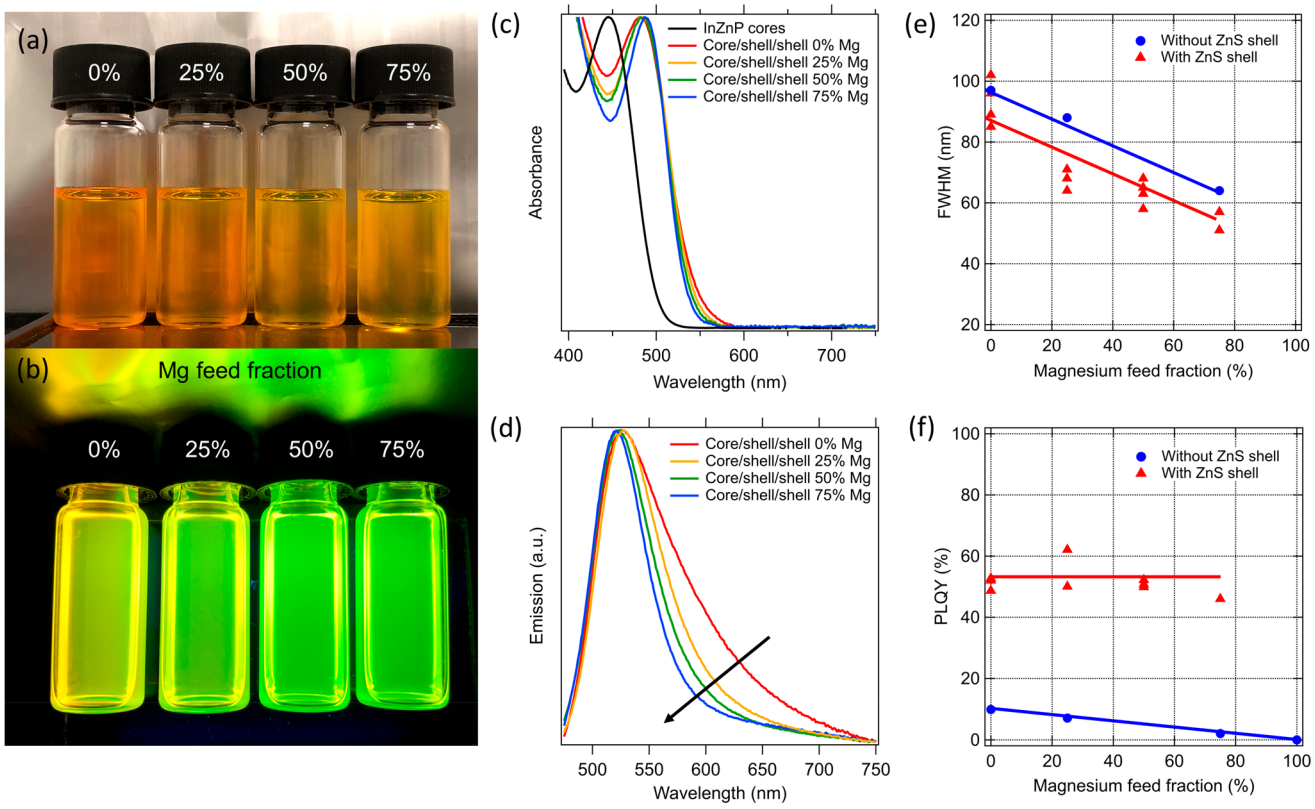

Figure 5. Photographs of dispersions of InZnP/Zn(Mg)Se/ZnS core−shell−shell QDs under ambient (a) and UV light (b). The change in color of the emission is clearly visible by eye, going from yellow for a pure ZnSe shell to green for samples with a high Mg feed fraction for the shell synthesis. (c) Absorption spectra of InZnP cores and InZnP/Zn(Mg)Se/ZnS core−shell−shell QDs (normalized to 1 for the first excitonic peak), showing a similar red-shift for all core−shell−shell QDs compared to the cores. The higher the Mg feed fraction, the sharper the absorbance peak. (d) Emission spectra of the InZnP/Zn(Mg)Se/ZnS core−shell−shell QDs (normalized to 1 for the emission peak) and (e) FWHM of the emission peak for different Mg feed fractions. The FWHM decreases strongly for increasing the feed fraction of Mg. This effect is enhanced when passivating the susceptible material with a protective ZnS shell. (f) Photoluminescence quantum yield vs Mg feed fraction with (red triangles) and without (blue circles) final ZnS shell. Only when growing the ZnS shell, QDs are stable enough to retain a high PLQY. Solid lines in (e) and (f) are a guide to the eye.

amount of ZnMgSe shell precursors) and an additional thin ZnS shell do show a systematic lattice expansion upon increasing the amount of Mg, as indicated by the shift of the XRD reflections to lower 2θ values in Figure 4. Hence, the incorporation of Mg in the shell indeed decreases the lattice mismatch. The peak in the XRD diffractograms around 25°, unexpected for zinc blende crystals, has been found more often in the literature for a variety of zinc blende materials[25,42−44] and can be assigned to metal−ligand complexes on the surface of the QDs.[43,44] We remark that the InZnP QD cores showed a lattice parameter similar to bulk InP, suggesting only little Zn was incorporated. ICP-OES and XPS revealed that the In:Zn ratio (6:1) was indeed much lower than the feed fraction (2:1). This leaves room for further improvement of the lattice matching. Yet, the expected lattice mismatch for the 50% Mg feed fraction in the shell is only 1.7%.

Figure 5 summarizes the optical properties of the InZnP/Zn(Mg)Se/ZnS QDs, synthesized according to the synthesis procedure reported. Figures 5a and 5b show photographs of samples prepared with 0−75% of magnesium feed fraction in the shell under ambient light and UV illumination, respectively. A clear color change is visible in Figure 5b, from yellow emission at 0% Mg to bright green emission at 75% Mg. Absorption spectra are plotted in Figure 5c. The absorption spectra for core−shell samples all showed a red-shift compared to the InZnP core only sample, possibly due to wave function delocalization over the shell.[45] The differences in the absorption spectra for different Mg feed ratios are small, but clearly noticeable. For an increased feed fraction of Mg the absorption spectra become sharper and shift slightly more to the red.

The emission spectra, displayed in Figure 5d, exhibit much larger differences for the different magnesium fractions. In contrast to the small red-shift of the absorption maximum, the PL maximum shifts to the blue for increasing Mg fractions, implying a reduced Stokes shift (see Figure S12 for a plot of the Stokes shift vs Mg fraction). At the same time, the photoluminescence spectra become much narrower, especially due to a decrease of the red tail of the emission peak. The FWHM vs Mg feed fraction is plotted in Figure 5e, and it was found to decrease from 90 nm without Mg to 50 nm for a 75% Mg feed fraction. As presented in Figure 5f, the PLQY of all samples was around 50% within error (red triangles). If the material was not protected by the final ZnS shell, the PLQY was much lower and decreased with increasing Mg fraction (blue circles in Figure 5f), probably as a result of rapid degradation of the ZnMgSe shell.

The relatively broad emission that characterizes InP-based QDs was recently addressed in several studies.[16,25,45,46] Especially the very thorough study by the Talapin group

https://dx.doi.org/10.1021/acsanm.0c00583
ACS Appl. Nano Mater. 2020, 3, 3859−3867

convincingly showed that the broad emission spectra are due to radiative recombination of delocalized conduction band electrons with localized holes.[16] Combined with strong electron−phonon coupling this explains the relatively large Stokes shift and the large FWHM. Temperature-dependent PL measurements on InP QDs[46] and on InP/ZnS and InP/ZnSe[25] indeed show structure in the emission spectra associated with trap emission at reduced temperatures. Janke et al.[16] associated the hole traps with structural disorder, e.g., as a result of a core−shell lattice mismatch, or in particular via the incorporation of substitutional Zn^{2+} in the InP core. The latter should form a shallow acceptor state that could trap holes and be responsible for the broadened and red-shifted emission.

The InZnP/ZnMgSe/ZnS QDs shown here exhibit very similar features as InP/ZnSe QDs. As plotted in Figure S12, the Stokes shift decreases with increasing amounts of Mg, and this Stokes shift correlates positively with the FWHM of the emission. This is in line with hole localization on shallow states just above the valence band and strong electron−phonon coupling associated with this hole localization. This would imply that the inclusion of Mg in the shell material reduces the number of hole traps and/or reduces the electron−phonon coupling. While all investigated samples contained Zn^{2+} in the core, and this likely did not change upon ZnMgSe shell growth, the decreasing lattice mismatch for higher Mg amounts in the shell could lead to reduced structural disorder at the core−shell interface. This was in fact the ansatz of this work.

The fact that the PLQY does not increase while the FWHM becomes narrower suggests a reduction of interfacial trap states, which can be explained by the fact that the shallow hole traps responsible for the broad emission are in fact radiative. In general, high PLQY often correlates with broad emission in InP/ZnSe QDs,[45] demonstrating the high efficiency of free electron−localized hole recombination for this system. Reducing the number of localized hole states thus results in a blue-shift and narrower emission lines but not in an increased PLQY.

The reported values for the PLQY and FWHM of the InZnP/ZnMgSe/ZnS QDs in this work are inferior to those of InP/ZnSe/ZnS QDs reported in recent literature. We consider that this may be because the InP/ZnSe/ZnS system has been extensively studied and optimized by a large number of research groups.[6,24−27,38,45] This optimization has not yet happened for the InZnP/ZnMgSe/ZnS QDs. The current work does show that it is possible to use ZnMgSe as a shell material with a smaller lattice mismatch than that of the commonly used ZnSe and ZnS shells. This offers increased flexibility in designing shell materials for InP QDs.

CONCLUSIONS

Magnesium selenide shells, alloyed with zinc to grow in the zinc blende crystal structure, were grown around indium zinc phosphide quantum dots in an attempt to improve lattice matching between the core and the shell material. To grow magnesium containing shells, we employed highly reactive organometallic precursors. The shell material was thereafter protected by a second zinc sulfide shell to increase the stability of the quantum dots. With this method we can reliably synthesize InZnP/ZnMgSe/ZnS QDs with variable Mg content in the shell and with reduced lattice mismatch. The inclusion of Mg in the shell results in much narrower emission features, which can be attributed to a reduced formation of shallow hole traps at the core−shell interface. These narrower emission features may be of large interest for the production of high quality phosphors for optoelectronic applications.

ASSOCIATED CONTENT

Supporting Information

The Supporting Information is available free of charge at https://pubs.acs.org/doi/10.1021/acsanm.0c00583.

Absorbance spectra for scaled-up syntheses, absorbance and emission spectra for core/shell QDs with and without intermediate purification step, shell synthesis methods with stearate precursors, electron diffraction patterns of ZnMgSe NCs, TEM images of ZnMgSe NCs with and without ZnS shell, EDX analysis on ZnMgSe/ZnS NCs, XPS and XRD data of InZnP/ZnMgSe QDs, HR-STEM image of an InZnP/ZnMgSe QD, reproducibility of the mentioned emission results, correlation between FWHM and Stokes shift of the emission peak (PDF)

AUTHOR INFORMATION

Corresponding Author

Arjan J. Houtepen − *Optoelectronic Materials Section, Faculty of Applied Sciences, Delft University of Technology, 2629HZ Delft, The Netherlands;* orcid.org/0000-0001-8328-443X; Email: A.J.Houtepen@tudelft.nl

Authors

Jence T. Mulder − *Optoelectronic Materials Section, Faculty of Applied Sciences, Delft University of Technology, 2629HZ Delft, The Netherlands;* orcid.org/0000-0002-4397-1347

Nicholas Kirkwood − *Optoelectronic Materials Section, Faculty of Applied Sciences, Delft University of Technology, 2629HZ Delft, The Netherlands;* orcid.org/0000-0002-7845-7081

Luca De Trizio − *Department of Nanochemistry, Istituto Italiano di Tecnologia (IIT), 16163 Genova, Italy;* orcid.org/0000-0002-1514-6358

Chen Li − *Electron Microscopy for Materials Science (EMAT), Department of Physics, University of Antwerp, 2020 Antwerp, Belgium;* orcid.org/0000-0001-9839-6100

Sara Bals − *Electron Microscopy for Materials Science (EMAT), Department of Physics, University of Antwerp, 2020 Antwerp, Belgium;* orcid.org/0000-0002-4249-8017

Liberato Manna − *Department of Nanochemistry, Istituto Italiano di Tecnologia (IIT), 16163 Genova, Italy;* orcid.org/0000-0003-4386-7985

Complete contact information is available at: https://pubs.acs.org/10.1021/acsanm.0c00583

Notes

The authors declare no competing financial interest.

ACKNOWLEDGMENTS

This project has received funding from the European Union's Horizon 2020 research and innovation programme under Grant Agreement No. 766900 (testing the large-scale limit of quantum mechanics). A.J.H. acknowledges support from the European Research Council Horizon 2020 ERC Grant Agreement No. 678004 (Doping on Demand). This research is supported by the Dutch Technology Foundation TTW, which is part of The Netherlands Organization for Scientific Research (NWO) and which is partly funded by Ministry of

Economic Affairs. The authors thank Wiel Evers for performing the TEM imaging and the EDX analysis. The authors also thank Lea Pasquale and Mirko Prato for their help with performing and analyzing the XPS measurements and Filippo Drago for the ICP measurements.

REFERENCES

(1) Alivisatos, A. P. Semiconductor Clusters, Nanocrystals, and Quantum Dots. *Science* **1996**, *271* (5251), 933−937.
(2) Bourzac, K. Quantum Dots Go on Display. *Nature* **2013**, *493* (7432), 283−283.
(3) Anikeeva, P. O.; Halpert, J. E.; Bawendi, M. G.; Bulović, V. Quantum Dot Light-Emitting Devices with Electroluminescence Tunable over the Entire Visible Spectrum. *Nano Lett.* **2009**, *9* (7), 2532−2536.
(4) Caruge, J. M.; Halpert, J. E.; Wood, V.; Bulović, V.; Bawendi, M. G. Colloidal Quantum-Dot Light-Emitting Diodes with Metal-Oxide Charge Transport Layers. *Nat. Photonics* **2008**, *2* (4), 247−250.
(5) Zhang, H.; Hu, N.; Zeng, Z.; Lin, Q.; Zhang, F.; Tang, A.; Jia, Y.; Li, L. S.; Shen, H.; Teng, F.; Du, Z. High-Efficiency Green InP Quantum Dot-Based Electroluminescent Device Comprising Thick-Shell Quantum Dots. *Adv. Opt. Mater.* **2019**, *7* (7), 1801602.
(6) Cao, F.; Wang, S.; Wang, F.; Wu, Q.; Zhao, D.; Yang, X. A Layer-by-Layer Growth Strategy for Large-Size InP/ZnSe/ZnS Core−Shell Quantum Dots Enabling High-Efficiency Light-Emitting Diodes. *Chem. Mater.* **2018**, *30* (21), 8002−8007.
(7) Sargent, E. H. Colloidal Quantum Dot Solar Cells. *Nat. Photonics* **2012**, *6* (3), 133−135.
(8) Crisp, R. W.; Pach, G. F.; Kurley, J. M.; France, R. M.; Reese, M. O.; Nanayakkara, S. U.; Macleod, B. A.; Talapin, D. V.; Beard, M. C.; Luther, J. M. Tandem Solar Cells from Solution-Processed CdTe and PbS Quantum Dots Using a ZnTe-ZnO Tunnel Junction. *Nano Lett.* **2017**, *17* (2), 1020−1027.
(9) Frasco, M.; Chaniotakis, N. Semiconductor Quantum Dots in Chemical Sensors and Biosensors. *Sensors* **2009**, *9* (9), 7266−7286.
(10) Silvi, S.; Credi, A. Luminescent Sensors Based on Quantum Dot−molecule Conjugates. *Chem. Soc. Rev.* **2015**, *44* (13), 4275−4289.
(11) Michalet, X. Quantum Dots for Live Cells, in Vivo Imaging, and Diagnostics. *Science* **2005**, *307* (5709), 538−544.
(12) Gao, X.; Cui, Y.; Levenson, R. M.; Chung, L. W. K.; Nie, S. In Vivo Cancer Targeting and Imaging with Semiconductor Quantum Dots. *Nat. Biotechnol.* **2004**, *22* (8), 969−976.
(13) McBride, J.; Treadway, J.; Feldman, L. C.; Pennycook, S. J.; Rosenthal, S. J. Structural Basis for Near Unity Quantum Yield Core/Shell Nanostructures. *Nano Lett.* **2006**, *6* (7), 1496−1501.
(14) Pan, J.; Shang, Y.; Yin, J.; De Bastiani, M.; Peng, W.; Dursun, I.; Sinatra, L.; El-Zohry, A. M.; Hedhili, M. N.; Emwas, A. H.; Mohammed, O. F.; Ning, Z.; Bakr, O. M. Bidentate Ligand-Passivated CsPbI3 Perovskite Nanocrystals for Stable Near-Unity Photoluminescence Quantum Yield and Efficient Red Light-Emitting Diodes. *J. Am. Chem. Soc.* **2018**, *140* (2), 562−565.
(15) Greytak, A. B.; Allen, P. M.; Liu, W.; Zhao, J.; Young, E. R.; Popović, Z.; Walker, B. J.; Nocera, D. G.; Bawendi, M. G. Alternating Layer Addition Approach to CdSe/CdS Core/Shell Quantum Dots with near-Unity Quantum Yield and High on-Time Fractions. *Chem. Sci.* **2012**, *3* (6), 2028.
(16) Janke, E. M.; Williams, N. E.; She, C.; Zherebetskyy, D.; Hudson, M. H.; Wang, L.; Gosztola, D. J.; Schaller, R. D.; Lee, B.; Sun, C.; Engel, G. S.; Talapin, D. V. Origin of Broad Emission Spectra in InP Quantum Dots: Contributions from Structural and Electronic Disorder. *J. Am. Chem. Soc.* **2018**, *140* (46), 15791−15803.
(17) Akkerman, Q. A.; Rainò, G.; Kovalenko, M. V.; Manna, L. Genesis, Challenges and Opportunities for Colloidal Lead Halide Perovskite Nanocrystals. *Nat. Mater.* **2018**, *17* (5), 394−405.
(18) Kim, J.-Y.; Yang, J.; Yu, J. H.; Baek, W.; Lee, C.-H.; Son, H. J.; Hyeon, T.; Ko, M. J. Highly Efficient Copper−Indium−Selenide Quantum Dot Solar Cells: Suppression of Carrier Recombination by Controlled ZnS Overlayers. *ACS Nano* **2015**, *9* (11), 11286−11295.
(19) Song, W.-S.; Yang, H. Efficient White-Light-Emitting Diodes Fabricated from Highly Fluorescent Copper Indium Sulfide Core/Shell Quantum Dots. *Chem. Mater.* **2012**, *24* (10), 1961−1967.
(20) Brichkin, S. B. Synthesis and Properties of Colloidal Indium Phosphide Quantum Dots. *Colloid J.* **2015**, *77* (4), 393−403.
(21) Chibli, H.; Carlini, L.; Park, S.; Dimitrijevic, N. M.; Nadeau, J. L. Cytotoxicity of InP/ZnS Quantum Dots Related to Reactive Oxygen Species Generation. *Nanoscale* **2011**, *3* (6), 2552.
(22) Gary, D. C.; Glassy, B. A.; Cossairt, B. M. Investigation of Indium Phosphide Quantum Dot Nucleation and Growth Utilizing Triarylsilylphosphine Precursors. *Chem. Mater.* **2014**, *26* (4), 1734−1744.
(23) Tessier, M. D.; De Nolf, K.; Dupont, D.; Sinnaeve, D.; De Roo, J.; Hens, Z. Aminophosphines: A Double Role in the Synthesis of Colloidal Indium Phosphide Quantum Dots. *J. Am. Chem. Soc.* **2016**, *138* (18), 5923−5929.
(24) Pietra, F.; Kirkwood, N.; De Trizio, L.; Hoekstra, A. W.; Kleibergen, L.; Renaud, N.; Koole, R.; Baesjou, P.; Manna, L.; Houtepen, A. J. Ga for Zn Cation Exchange Allows for Highly Luminescent and Photostable InZnP-Based Quantum Dots. *Chem. Mater.* **2017**, *29* (12), 5192−5199.
(25) Kim, Y.; Ham, S.; Jang, H.; Min, J. H.; Chung, H.; Lee, J.; Kim, D.; Jang, E. Bright and Uniform Green Light Emitting InP/ZnSe/ZnS Quantum Dots for Wide Color Gamut Displays. *ACS Appl. Nano Mater.* **2019**, *2* (3), 1496−1504.
(26) Li, Y.; Hou, X.; Dai, X.; Yao, Z.; Lv, L.; Jin, Y.; Peng, X. Stoichiometry-Controlled InP-Based Quantum Dots: Synthesis, Photoluminescence, and Electroluminescence. *J. Am. Chem. Soc.* **2019**, *141* (16), 6448−6452.
(27) Won, Y.-H.; Cho, O.; Kim, T.; Chung, D.-Y.; Kim, T.; Chung, H.; Jang, H.; Lee, J.; Kim, D.; Jang, E. Highly Efficient and Stable InP/ZnSe/ZnS Quantum Dot Light-Emitting Diodes. *Nature* **2019**, *575* (7784), 634−638.
(28) Hanifi, D. A.; Bronstein, N. D.; Koscher, B. A.; Nett, Z.; Swabeck, J. K.; Takano, K.; Schwartzberg, A. M.; Maserati, L.; Vandewal, K.; van de Burgt, Y.; Salleo, A.; Alivisatos, A. P. Redefining Near-Unity Luminescence in Quantum Dots with Photothermal Threshold Quantum Yield. *Science* **2019**, *363* (6432), 1199−1202.
(29) Chen, O.; Zhao, J.; Chauhan, V. P.; Cui, J.; Wong, C.; Harris, D. K.; Wei, H.; Han, H.-S.; Fukumura, D.; Jain, R. K.; Bawendi, M. G. Compact High-Quality CdSe−CdS Core−shell Nanocrystals with Narrow Emission Linewidths and Suppressed Blinking. *Nat. Mater.* **2013**, *12* (5), 445−451.
(30) Shendre, S.; Delikanli, S.; Li, M.; Dede, D.; Pan, Z.; Ha, S. T.; Fu, Y. H.; Hernández-Martínez, P. L.; Yu, J.; Erdem, O.; Kuznetsov, A. I.; Dang, C.; Sum, T. C.; Demir, H. V. Ultrahigh-Efficiency Aqueous Flat Nanocrystals of CdSe/CdS@$Cd_{1-x}Zn_xS$ Colloidal Core/Crown@alloyed-Shell Quantum Wells. *Nanoscale* **2019**, *11* (1), 301−310.
(31) Donegá, C. D. M. Synthesis and Properties of Colloidal Heteronanocrystals. *Chem. Soc. Rev.* **2011**, *40* (3), 1512−1546.
(32) Pietra, F.; Koole, R.; Grozema, F. C.; Prato, M.; De Trizio, L.; Baesjou, P. J.; Renaud, N.; Houtepen, A. J.; Manna, L.; Hoekstra, A. W. Tuning the Lattice Parameter of In x Zn y P for Highly Luminescent Lattice-Matched Core/Shell Quantum Dots. *ACS Nano* **2016**, *10* (4), 4754−4762.
(33) Madelung, O. *Semiconductors: Data Handbook*, 3rd ed.; Springer: Berlin, 2004.
(34) Yoshikawa, A.; Matsunami, H.; Nanishi, Y. Development and Applications of Wide Bandgap Semiconductors. In *Wide Bandgap Semiconductors*; Springer: Berlin, 2007; p 8.
(35) Elsayed, H.; Olguín, D.; Cantarero, A.; Hernández-Calderón, I. Ab Initio Structural and Electronic Band-Structure Study of MgSe. *Phys. Status Solidi B* **2015**, *252* (4), 663−669.
(36) Sohel, M.; Muñoz, M.; Tamargo, M. C. Molecular Beam Epitaxial Growth and Characterization of Zinc-Blende ZnMgSe on InP (001). *Appl. Phys. Lett.* **2004**, *85* (14), 2794−2796.

https://dx.doi.org/10.1021/acsanm.0c00583
ACS Appl. Nano Mater. 2020, 3, 3859−3867

(37) Kirkwood, N.; De Backer, A.; Altantzis, T.; Winckelmans, N.; Longo, A.; Antolinez, F. V.; Rabouw, F. T.; De Trizio, L.; Geuchies, J. J.; Mulder, J. T.; Renaud, N.; Bals, S.; Manna, L.; Houtepen, A. J. Locating and Controlling the Zn Content in In(Zn)P Quantum Dots. *Chem. Mater.* **2020**, *32* (1), 557−565.
(38) Ramasamy, P.; Kim, N.; Kang, Y.-S.; Ramirez, O.; Lee, J.-S. Tunable, Bright, and Narrow-Band Luminescence from Colloidal Indium Phosphide Quantum Dots. *Chem. Mater.* **2017**, *29* (16), 6893−6899.
(39) Boldt, K.; Schwarz, K. N.; Kirkwood, N.; Smith, T. A.; Mulvaney, P. Electronic Structure Engineering in ZnSe/CdS Type-II Nanoparticles by Interface Alloying. *J. Phys. Chem. C* **2014**, *118* (24), 13276−13284.
(40) Grabolle, M.; Spieles, M.; Lesnyak, V.; Gaponik, N.; Eychmüller, A.; Resch-Genger, U. Determination of the Fluorescence Quantum Yield of Quantum Dots: Suitable Procedures and Achievable Uncertainties. *Anal. Chem.* **2009**, *81* (15), 6285−6294.
(41) Li, L. S.; Pradhan, N.; Wang, Y.; Peng, X. High Quality ZnSe and ZnS Nanocrystals Formed by Activating Zinc Carboxylate Precursors. *Nano Lett.* **2004**, *4* (11), 2261−2264.
(42) Mirzai, H.; Nordin, M. N.; Curry, R. J.; Bouillard, J.-S.; Zayats, A. V.; Green, M. The Room Temperature Phosphine-Free Synthesis of near-Infrared Emitting HgSe Quantum Dots. *J. Mater. Chem. C* **2014**, *2* (12), 2107−2111.
(43) Wegner, K. D.; Pouget, S.; Ling, W. L.; Carrière, M.; Reiss, P. Gallium − a Versatile Element for Tuning the Photoluminescence Properties of InP Quantum Dots. *Chem. Commun.* **2019**, *55* (11), 1663−1666.
(44) Carević, M. V.; Čomor, M. I.; Mitrić, M. N.; Barudžija, T. S.; Ahrenkiel, S. P.; Abazović, N. D. The Influence of Reaction Media on $CdIn_2S_4$ and $ZnIn_2S_4$ Nanocrystallite Formation and Growth of Mesocrystal Structures. *CrystEngComm* **2015**, *17* (44), 8492−8499.
(45) Hahm, D.; Chang, J. H.; Jeong, B. G.; Park, P.; Kim, J.; Lee, S.; Choi, J.; Kim, W. D.; Rhee, S.; Lim, J.; Lee, D. C.; Lee, C.; Char, K.; Bae, W. K. Design Principle for Bright, Robust, and Color-Pure InP/$ZnSe_xS_{1-x}$/ZnS Heterostructures. *Chem. Mater.* **2019**, *31* (9), 3476−3484.
(46) Cho, E.; Kim, T.; Choi, S.; Jang, H.; Min, K.; Jang, E. Optical Characteristics of the Surface Defects in InP Colloidal Quantum Dots for Highly Efficient Light-Emitting Applications. *ACS Appl. Nano Mater.* **2018**, *1* (12), 7106−7114.

https://dx.doi.org/10.1021/acsanm.0c00583
ACS Appl. Nano Mater. 2020, 3, 3859−3867